Acta Mech
DOI 10.1007/s00707-011-0568-x

Jinkyu Yang · Sachith Dunatunga · Chiara Daraio

Amplitude-dependent attenuation of compressive waves in curved granular crystals constrained by elastic guides

Received: 22 March 2011

Abstract We study the wave propagation in a curved chain of spherical particles constrained by elastic guides under the axial impact of a falling mass. We characterize the force transmission properties of the chain by varying the striker's mass and the chain's curvature. Experimental tests demonstrate amplitude-dependent attenuation of compressive waves propagating through the curved chain. In particular, we observe that the curved systems present an improved transmission of small dynamic disturbances relative to that of strong excitations, resulting from the close interplay between the granular particles and the softer elastic medium. We also find that the transmission of the compressive waves through the chains is dependent on the initial curvature imposed to the system. Numerical simulations, based on an approach that combines discrete element and finite element methods, corroborate the experimental results. The findings suggest that hybrid structures composed of granular particles and linear elastic media can be employed as new passive acoustic filtering materials that selectively transmit or mitigate excitations in a desired range of pressure amplitudes.

1 Introduction

Chains of granular particles in elastic contact with each other (also defined as one-dimensional granular crystals) have been broadly studied to control compressive excitations [1–9]. Given external loads, such as impulse and harmonic excitations, these systems can be tuned to respond in different acoustic regimes, ranging from linear, weakly nonlinear, to highly nonlinear states [1]. It has been shown that the alteration of the dynamic regime can be easily made by manipulating precompression initially applied to the granular crystals [1,3]. Under strong precompression, these closely packed granular crystals exhibit acoustic band gaps with distinctive pass and forbidden frequency bands, resulting from linear dispersion [4,10]. In the case of zero or very weak precompression, one of the most studied characteristics of granular crystals is the ability to support the formation and propagation of highly nonlinear acoustic waves in the form of solitary waves [1,5]. These solitary waves are essentially energy pulses, mostly confined within the wave length of about five particle diameters in case of monodispersed chains, that derive from a balance between dispersive and nonlinear effects [1]. They are characterized by unique physical properties, such as robustness, amplitude-dependent wave propagation speed, and high energy intensity [1,11,12].

J. Yang
Mechanical Engineering, University of South Carolina, 300 Main Street, A224, Columbia, SC 29208, USA

J. Yang · S. Dunatunga · C. Daraio (✉)
Engineering and Applied Science, California Institute of Technology,
1200 E. California Blvd., MC 105-50, Pasadena, CA 91125, USA
E-mail: daraio@caltech.edu
Tel.: +1-626-395-4479
Fax: +1-626-449-6359

Solitary waves propagating in granular crystals have been proposed for several engineering applications, such as nonlinear lenses for acoustic imaging [12], sound scramblers [6], and actuators and sensors for nondestructive evaluations [13,14]. In particular, previous studies have suggested that nonlinear granular crystals can act as effective media for shock/impact mitigation, owing to their ability to trap [7,15], localize [16,17], redirect [18,19], and redistribute energy [20]. These capabilities are based on the complex dynamic behavior of granular chains composed of particles of different materials and geometry. The presence of dissipation, evident in experimental studies of granular crystals, provides the additional means for mitigating external impacts. Several reports have recently provided different theoretical models to capture the force decay observed in experiments [21–23].

In this manuscript, we study the dynamic response of a curved chain of spherical particles constrained by structurally deformable elastic guides. We excite compressive waves in this system with axial impacts of different falling masses. We vary the chain's initial curvature imposed by the elastic guides to study the attenuation effects related to the structural arrangements of granules and their interaction with the elastic guides. This combined system of granular particles and linear support media allows studying the effects of structural bending of the elastic supports on the propagation of nonlinear waves in the granular chains. We find that the transmission of the compressive waves through the chains is dependent on the initial curvature imposed to the system. More notably, we show that the curved systems flex dynamically in response to an impact and present an improved transmission of small dynamic disturbances relative to that of strong excitations. This effectively results in an amplitude-dependent filtering of acoustic excitations. Such an amplitude-dependent response is an interesting characteristic of this hybrid system, resulting from the close interplay between the granular crystal and the linear elastic guides.

To study the wave propagation in this coupled system of nonlinear and linear media, we perform experiments using a high-speed camera and a force sensor and verify the measurements with a numerical model that combines discrete element (DE) and finite element (FE) methods. In previous studies, the DE model with the Hertzian contact among particles has been widely used to simulate the formation and propagation of solitary waves in one-dimensional granular crystals [1–3,5,7,10,11]. For two- or three-dimensional granular crystals with oblique interaction between particles, we need a full-fledged DE method to accommodate both axial and tangential interactions between particles. In this study, we introduce a DE model based on the Hertzian–Mindlin contact law to describe the dynamics of granular particles in a curved chain under external impact [24,25]. We formulate the normal and tangential contact forces with dissipative terms using the Lagrangian approach described in the Cundall [26] and Tsuji models [27]. We also apply this DE model with some modifications to account for the contact force between the particles and the elastic guides. Using the combined DE and FE model, we verify the amplitude-dependent behavior of the coupled "nonlinear" granular and the "linear" elastic media. We find that the numerical results based on the combined model corroborate the experimental results. The findings of this work suggest the use of hybrid linear-nonlinear systems in engineering applications, such as tunable protective materials that selectively allow or forbid the transmission of external impacts, and novel acoustic devices for filtering and redirecting waves and mitigating vibrations.

2 Experimental setup

We assemble a vertical one-dimensional (1D) granular crystal composed of 21 spherical particles in a holder consisting of four polytetrafluoroethylene (PTFE) tubes. The particles are made from stainless steel (type 440C, McMaster-Carr), with a radius $R = 9.53$ mm, mass $m = 28.2$ g, elastic modulus $E = 200$ GPa, and Poisson's ratio $\upsilon = 0.28$. The supporting tubes have a radius $R_G = 6.35$ mm, density $\rho_G = 4{,}302\,\mathrm{kg/m^3}$, elastic modulus $E_G = 0.46$ GPa, and Poisson's ratio $\upsilon_G = 0.46$. The tubes are held in place by two steel plates located at the top and bottom of the chain (Fig. 1). The choice of a soft material (PTFE) for the supporting tubes allows bending the chain to a desired initial curvature and to flex dynamically upon impact. In addition, PTFE ensures a low-friction coefficient between the particles and the tubes. An initial curvature is imposed on the PTFE guides by controlling the position of the top and bottom steel plates. A custom-made linkage structure provides the top support with translational and rotational degrees of freedom, allowing the system to dynamically bend under impact. The curvature of the bent chain is represented by an offset Δ measured from the centerline of the assembled structure (see Fig. 1a). We test three differently curved chains ($\Delta = 11.4$, 24.1, and 40.5 mm) and a straight chain as a reference configuration. In the case of a straight chain, the guiding rails are made of stainless steel to firmly restrict the lateral motions of the granular particles (Fig. 1b).

We apply various impacts to the granular chain using 13 different strikers made of stainless steel cylinders. The length L of the cylinders varies from 6.35 to 304.8 mm, while their diameters are kept constant at 19.1 mm.

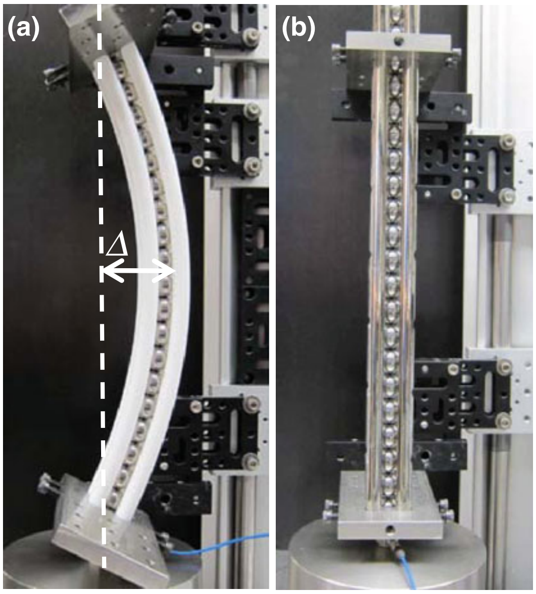

Fig. 1 Experimental setup. **a** Curved configuration of a granular chain composed of 21 stainless steel beads ($R = 9.53$ mm) constrained by 4 PTFE tubes. The initial curvature of the bent chain is represented by an offset Δ from the centerline (*dashed line*). **b** Straight configuration of identical beads confined by 4 stainless steel rods. The height of the straight chain is 0.40 m

These sizes correspond to a range of striker masses M from 14.1 to 678 g, which are 0.5–24 times the mass of an individual bead. The striker impact is designed to directly contact only the top bead of the granular chain, without touching the guiding rails. For an accurate control of the impact velocity, the striker is released from a 1-cm drop height using a DC-powered solenoid [28]. We limit the drop height to 1 cm to exclude the possible onset of plasticity at or around the contact region [25]. The force transmission through the granular chain is measured by a commercial force sensor (PCB Piezotronics 208C04) located at the bottom of the chain, which is mounted on a massive block that simulates a rigid wall. The impact cap of the sensor is made of hardened 17-4 PH (H900) stainless steel, which we assume to have identical density, elastic modulus, and Poisson's ratio to those of the chain composing beads. The sensor is connected to a data acquisition board (National Instrument PCI-6115) to collect force-time history of transmitted waves. To capture the dynamic bending of the guiding rods, a high-speed camera (Vision Research Phantom V12) is used at a sampling frequency of 20 kHz and with 0.066 mm/pixel resolution. We perform digital image processing on the acquired snapshot images to enlarge the effective resolution of the area of interest [29].

3 Numerical approach

In previous studies, one-dimensional (1D) granular crystals have been successfully modeled as chains of point-masses connected by nonlinear springs based on Hertzian contact interaction [1–3,5,7,10,11]. In such discrete element models (DE), the particles are considered as rigid bodies and dissipative losses are neglected. It was shown that the dynamics of short granular chains could be well represented without the need of fitting parameters [3,5–7]. In this study, we extend this 1D model to a full-fledged DE model, which accounts for both normal and tangential contact forces with dissipative terms, to capture the oblique interactions between particles in curved granular chains. The dynamic behavior of the linear elastic guides is simulated using the finite element (FE) model, by discretizing the elastic guides into Bernoulli–Euler beam elements [30,31].

3.1 Particle dynamics in the curved granular crystal

We first describe the equations of particles' motion in the DE model using Newtonian mechanics, following the motion of individual particles [1,27]. The schematic diagram of the granular particles confined by elastic guides is illustrated in Fig. 2. In this closely packed granular chain, the increment of normal approach between

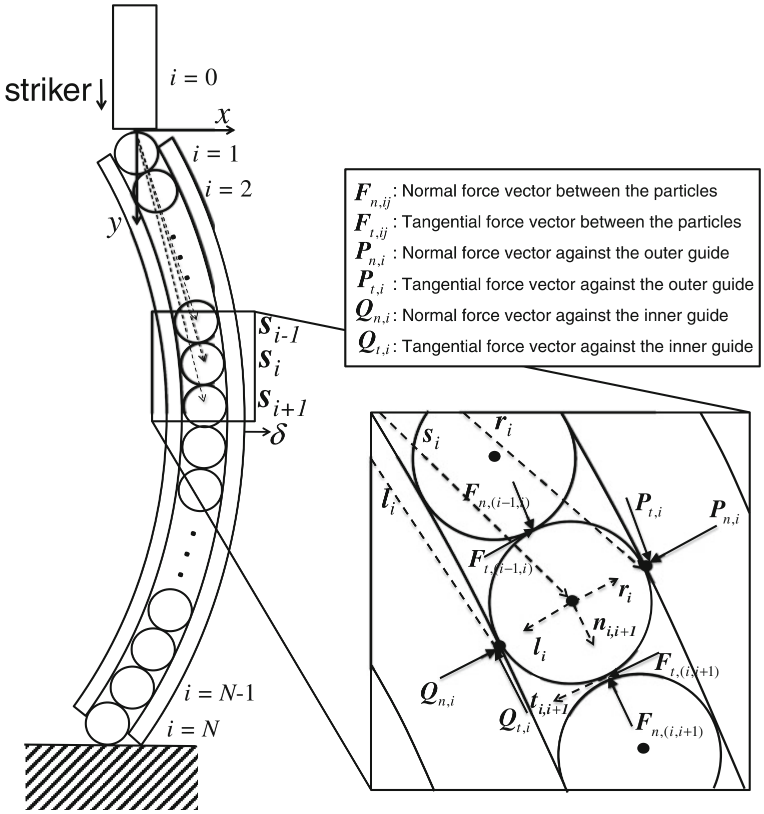

Fig. 2 Schematic diagram of granular particles confined by linear elastic guides. *Inset* shows a free body diagram of the ith particle under the normal and tangential forces exerted by neighboring beads and contacting guides. Here *dotted arrows* represent location vectors of contact points, while *solid arrows* denote force vectors

the neighboring ith and jth particles can be written as

$$\delta_{n,ij} = \left[|\boldsymbol{s}_i - \boldsymbol{s}_j| - (R_i + R_j)\right]_+ . \tag{1}$$

Here, $\boldsymbol{s}_i$ is the location vector of the ith particle's center with respect to the origin, which is the contact point between the cylindrical striker and the rigid wall (see Fig. 2). We represent the striker with index $i = 0$, and the total number of beads composing the granular crystal N is 21 in this study. The bracket $[x]_+$ takes only positive values and returns 0 if $x < 0$. This means that we consider only compressive interactions of neighboring particles, since there exists no tensile strength between granules.

The approaching velocity between particles at the contact point can be expressed by superposing translational and rotational velocity components:

$$\dot{\boldsymbol{\delta}}_{ij} = \dot{\boldsymbol{s}}_i - \dot{\boldsymbol{s}}_j - (R_i\boldsymbol{\omega}_i + R_j\boldsymbol{\omega}_j) \times \hat{\boldsymbol{n}}_{ij}, \quad \hat{\boldsymbol{n}}_{ij} = \frac{\boldsymbol{s}_i - \boldsymbol{s}_j}{|\boldsymbol{s}_i - \boldsymbol{s}_j|}, \tag{2}$$

where $(\dot{\cdot})$ denotes a time derivative, $\boldsymbol{\omega}_i$ is angular velocity of the ith particle, and $\hat{\boldsymbol{n}}_{ij}$ is the unit normal vector from the center of the ith particle to that of the jth particle (see the inset of Fig. 2). In Eqs. (1) and (2), $R_i = 0$ and $|\boldsymbol{\omega}_i| = 0$, when ith particle is replaced by the cylindrical striker or the wall (i.e., flat-headed sensor in this study). Accordingly, the normal and tangential speeds at the contact point are given by:

$$\dot{\delta}_{n,ij} = \dot{\boldsymbol{\delta}}_{ij} \cdot \hat{\boldsymbol{n}}_{ij} = (\dot{\boldsymbol{s}}_i - \dot{\boldsymbol{s}}_j) \cdot \hat{\boldsymbol{n}}_{ij}, \quad \dot{\delta}_{t,ij} = \dot{\boldsymbol{\delta}}_{ij} \cdot \hat{\boldsymbol{t}}_{ij}, \tag{3}$$

where $\hat{\boldsymbol{t}}_{ij}$ is the unit tangential vector in the clock-wise direction at the contact point $\left(\hat{\boldsymbol{t}}_{ij} \perp \hat{\boldsymbol{n}}_{ij}\right)$, and the subscripts n and t denote the normal and tangential components. Based on the tangential velocity at the contact point, the tangential displacement $\delta_{t,ij}$ can be calculated by

$$\delta_{t,ij} = \int \dot{\boldsymbol{\delta}}_{ij} \cdot \hat{\boldsymbol{t}}_{ij} \mathrm{d}t. \tag{4}$$

Given these displacement and velocity components at the contact point, we can derive the normal and tangential contact forces between neighboring particles using the Hertz–Mindlin contact law [24,25]. We begin with calculating the normal contact forces. Based on the damped Hertzian contact relationship [27], the nonlinear interaction between adjacent particles can be expressed:

$$\boldsymbol{F}_{n,ij} = -\left(A_{ij}\delta_{n,ij}^{3/2} + \gamma_{n,ij}\dot{\delta}_{n,ij}\right)\hat{\boldsymbol{n}}_{ij}, \tag{5}$$

where $\boldsymbol{F}_{n,ij}$ denotes a compressive force between the ith and jth elements, which is composed of the nonlinear Hertzian force with the coefficient A_{ij} and the normal dissipative force with damping coefficient $\gamma_{n,ij}$. The Hertzian coefficient A_{ij} is dictated by the Young's modulus (E), Poisson's ratio (v), and the radius (R) of the two neighboring materials as given by

$$\begin{aligned} A_{ij} &= \tfrac{4}{3}R_{ij}^{1/2}E_{ij}, \\ R_{ij} &= \tfrac{R_iR_j}{R_i+R_j},\ E_{ij} = \left(\tfrac{1-v_i^2}{E_i} + \tfrac{1-v_j^2}{E_j}\right)^{-1}. \end{aligned} \tag{6}$$

As for the normal damping, Tsuji et al. derived the damping coefficient $\gamma_{n,ij}$ based on the restitutional properties of particles:

$$\gamma_{n,ij} = \alpha_n(m_{ij}A_{ij})^{1/2}\delta_{n,ij}^{1/4}. \tag{7}$$

Here, m_{ij} is the effective mass between the contacting particles (i.e, $m_{ij} = m_im_j/(m_i + m_j)$), and α_n is the empirical constant determined by the coefficient of restitution (e), which is defined as the ratio of rebounding particle velocity to the incident one under the collision of particles. The coefficient of restitution for stainless steel spheres is reported in the range of $0.97 \sim 0.99$ [32,33]. Thus, we select $\alpha_n = 0.01$ in this study, which corresponds to the restitution coefficient $e \geq 0.95$ according to the relation between α_n and e in [27]. In Eq. (7), it is notable that the damping force is proportional to $\delta_{n,ij}^{1/4}$, implying that the more energy is dissipated under the larger axial displacement between particles. This also guarantees zero energy dissipation among the particles when they lose contact.

To accommodate the tangential traction when the particles are interacting obliquely, we use a linear damped spring model with a friction element [24,25]. In this model, the tangential force is represented by an incremental spring that stores energy from the relative tangential motion, resulted from the elastic tangential deformation of the particle surface. We also add the fictional force component proportional to the tangential velocity in order to include dissipative effects. Mathematically, the tangential force can be expressed as

$$\boldsymbol{F}_{t,ij} = -\left(K_{ij}\delta_{t,ij} + \gamma_{t,ij}\dot{\delta}_{t,ij}\right)\hat{\boldsymbol{t}}_{ij}, \tag{8}$$

where K_{ij} and $\gamma_{t,ij}$ are the tangential stiffness and damping coefficients. If no-slip occurs at the contact interface, K_{ij} can be analytically derived based on the Mindlin contact law [24,27]:

$$\begin{aligned} K_{ij} &= 8R_{ij}^{1/2}G_{ij}\delta_{n,ij}^{1/2}, \\ G_{ij} &= \left(\frac{2-v_i}{G_i} + \frac{2-v_j}{G_j}\right)^{-1}, \end{aligned} \tag{9}$$

where G_i is the shear modulus of the ith particle, which can be obtained by $G_i = E_i/2(1 + v_i)$ for isotropic materials. In Eq. (9), we find that the tangential stiffness is proportional to the square root of the axial displacement $\delta_{n,ij}$. This implies that the tangential force is dependent on the normal contact force, while the normal contact force is independent of the tangential force (see Eq. (5)). The Eq. (9) is derived under the assumption of "no-slip" condition at the contact interface. In reality, the contact surface starts to slip after a certain threshold of the tangential force. Thus, we limit the maximum tangential force of the linear spring component by the Coulomb frictional limit:

$$\max(K_{ij}\delta_{t,ij}) = \mu|\boldsymbol{F}_{n,ij}|, \tag{10}$$

where μ is the static friction coefficient. This means that above the Coulomb frictional limit, the particles start to slide irrespective of the tangential displacement $\delta_{t,ij}$. In this study, we use $\mu = 0.099$ for the static friction at the stainless steel /stainless steel interface [34].

For the tangential damping, we introduce a mathematical formula similar to the normal damping coefficient in Eq. (7) [27]. The tangential damping coefficient can be expressed as follows:

$$\gamma_{t,ij} = \alpha_t (m_{ij} A_{ij})^{1/2} \delta_{n,ij}^{1/4} = \frac{\alpha_t}{\alpha_n} \gamma_{n,ij}, \tag{11}$$

where α_t is the empirical constant for tangential damping, determined by the degree of frictional loss during the tangential interaction between particles. Due to the difficulty in relating α_t to any measurable physical quantities, Tsuji et al. assumed $\alpha_t = \alpha_n$. In this study, we select $\alpha_t = 10\alpha_n$ to match the experimental results, specifically the shape of the solitary waves propagating in the curved chain ($\Delta = 40.5\,\text{mm}$) under the largest mass impact ($m = 679\,\text{g}$).

3.2 Interaction between the granules and the elastic guides

The lateral supporting forces exerted on a sphere by the right- and left-hand linear guides are regulated by the modified Hertzian law for "sphere–cylinder" contact [35]. For the sake of brevity, the three-dimensional interplay of the guiding rails and the granular chain is simplified to two-dimensional representation. The relative normal displacements between the ith particle and the right-hand and left-hand guides are

$$\begin{aligned} \delta_{n,i}^{\text{right}} &= [|\boldsymbol{s}_i - \boldsymbol{r}_i| - R_i]_+, \\ \delta_{n,i}^{\text{left}} &= [|\boldsymbol{s}_i - \boldsymbol{l}_i| - R_i]_+, \end{aligned} \tag{12}$$

where $\boldsymbol{r}_i$ and $\boldsymbol{l}_i$ are the location vectors to the sphere's contact points with the right-hand and left-hand guides (Fig. 2).

We can calculate the normal and tangential forces between the particles and the elastic guides by employing the same approach used to derive the contact forces between the spherical particles in the chain. However, we need to modify the stiffness and damping coefficients corresponding to the "sphere–cylinder" contact instead of "sphere–sphere" configuration. Thus, we replace the Hertzian contact coefficient A_{ij} in "sphere–sphere" contact (see Eq. (6)) with a new coefficient B_i, which represents the contact between the ith sphere and the adjoined cylindrical guide. According to the expanded Hertzian contact law under "sphere–cylinder" contact [35], the modified Hertzian coefficient B_i can be given by:

$$\begin{aligned} B_i &= \frac{4}{3}(\lambda R_i)^{1/2} E', \\ E' &= \left(\frac{1-v_i^2}{E_i} + \frac{1-v_{\mathrm{G}}^2}{E_{\mathrm{G}}} \right)^{-1}, \end{aligned} \tag{13}$$

where subscript G denotes the material properties of the guiding tubes. Comparing Eqs. (6) and (13), the modified Hertzian coefficient B_i is similar to the regular Hertzian coefficient A_{ij}, except that λ is included in the equation. The coefficient λ represents an elliptical contact area formed by the "sphere–cylinder" contact, which is a function of the radii of the spherical and the cylindrical members. Based on the elliptical integral table in [35], we obtain $\lambda = 0.656$ given the dimensions of the spheres and the elastic guides ($R_i = 9.53\,\text{mm}$ and $R_{\mathrm{G}} = 6.35\,\text{mm}$) as described in Sect. 2.

According to the Hertz–Mindlin contact law, the tangential contact force is affected by the normal contact force, as briefly mentioned in the previous section. Thus, to account for the "sphere–cylinder" contact between the granules and the elastic guides, we need to revise the stiffness and damping coefficients in the tangential force expression in Eq. (8) using the modified Hertzian coefficient. In addition, we replace the static friction coefficient in Eq. (10) with $\mu = 0.04$, which is a conventional static frictional coefficient between stainless steel and PTFE materials.

Taking all the axial and tangential force components into account, the acceleration of the ith particle can be determined by the relation

$$\ddot{\boldsymbol{s}}_i = \frac{\sum (\boldsymbol{F}_{n,ij} + \boldsymbol{F}_{t,ij} + \boldsymbol{P}_{n,i} + \boldsymbol{P}_{t,i} + \boldsymbol{Q}_{n,i} + \boldsymbol{Q}_{t,i})}{m_i} + \boldsymbol{g}, \tag{14}$$

where $\boldsymbol{P}_i$ and $\boldsymbol{Q}_i$ denote the forces exerted on the ith particle by the left-hand and right-hand beam elements (see Fig. 2). We include gravity $\boldsymbol{g}$, considering the weight of granular particles.

The rotational motion of the beads can be described based on the conservation of angular momentum. The equilibrium equation of rotational motion is as follows:

$$\dot{\boldsymbol{\omega}}_i = \frac{\sum R_i \left(\hat{\boldsymbol{n}}_{ij} \times \boldsymbol{F}_{t,ij} + \hat{\boldsymbol{r}}_{ij} \times \boldsymbol{P}_{t,i} + \hat{\boldsymbol{l}}_{ij} \times \boldsymbol{Q}_{t,i} \right)}{I_i}, \tag{15}$$

where I_i is the rotational moment of inertia of the ith granule, and $\hat{\boldsymbol{r}}_{ij}$ and $\hat{\boldsymbol{l}}_{ij}$ are the unit vector from the center of the ith particle to its contact point with the left-hand and right-hand elastic guides (see Fig. 2).

3.3 Finite element model of the elastic guides

We use FE analysis to model the curved guides via a single array of beam elements. Each element has two nodes with three degrees of freedom in axial, shear, and rotational directions. The governing equations of motion for the right-hand and left-hand guiding structures can be expressed in a linear algebraic form as

$$\begin{aligned} [\boldsymbol{M}^{\mathrm{r}}]\ddot{\boldsymbol{r}} &= [\boldsymbol{K}^{\mathrm{r}}]\boldsymbol{r} + (\boldsymbol{P}_n + \boldsymbol{P}_t), \\ [\boldsymbol{M}^{\mathrm{l}}]\ddot{\boldsymbol{l}} &= [\boldsymbol{K}^{\mathrm{l}}]\boldsymbol{l} + (\boldsymbol{Q}_n + \boldsymbol{Q}_t), \end{aligned} \tag{16}$$

where the matrices $[\boldsymbol{M}^{\mathrm{r}}]$ and $[\boldsymbol{K}^{\mathrm{r}}]$ are the global mass and stiffness matrices of the right-hand elastic guide, while $[\boldsymbol{M}^{\mathrm{l}}]$ and $[\boldsymbol{K}^{\mathrm{l}}]$ are for the left-hand elastic guide. Note that the force vectors $\boldsymbol{P}_n, \boldsymbol{P}_t, \boldsymbol{Q}_n$, and $\boldsymbol{Q}_t$ are the contact forces applied by the particles in the granular crystal. These force components are governed by both granular particle movements (denoted by displacement vector $\boldsymbol{s}_i$) and the elastic guides deflections (denoted by $\boldsymbol{r}_i$ and $\boldsymbol{l}_i$). Thus, the equilibrium equations in Eqs. (14)–(16) are linked together, describing the coupling mechanism of the nonlinear granular media and the linear elastic guides. These ordinary differential equations are solved with the explicit Runge–Kutta integration scheme in MATLAB® [36].

4 Results and discussion

4.1 Deflection of linear elastic guides

We first study the global deflection of the linear elastic guides in response to dynamic impact excitations. In experiments, we use a high-speed camera to measure the dynamic deflection (δ) of the right-hand guide from its static equilibrium position (see the inset of Fig. 3). We compare the experimental measurements with numerical results based on our combined DE–FE method. Figure 3 shows the deflection-time history of the system, when the chain is impacted by the largest striker ($M = 678$ g) under the initial curvature of

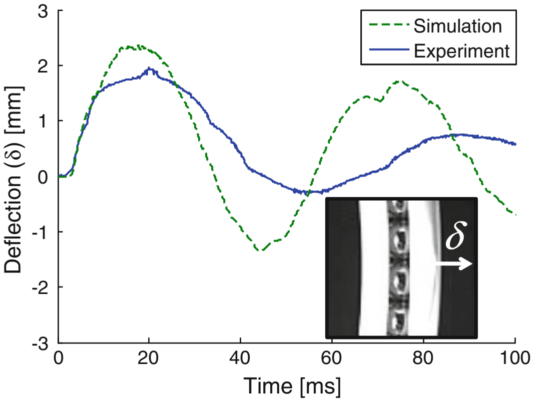

Fig. 3 Deflection curves of the guiding tube. The *solid line* represents experimental measurements of dynamic deflection δ of the right-hand guide from its static position via the high-speed camera (*inset* showing a still shot image). Here, the striker used is 678 g heavy, and initial offset of the bent chain is 40.5 mm. The *dotted line* denotes the numerical result based on the DE–FE method

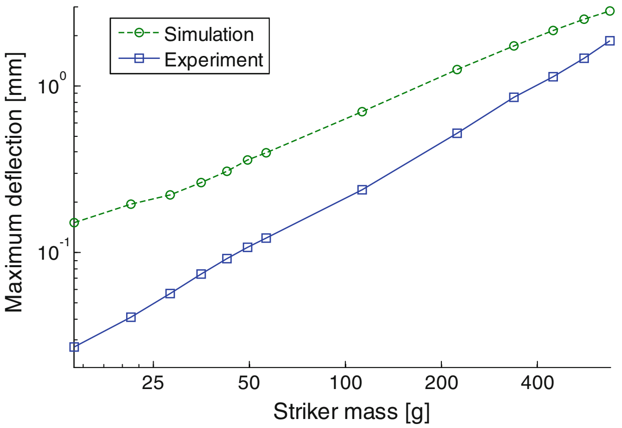

Fig. 4 Experimental and numerical curves of maximum deflection of linear elastic guides as a function of striker mass. For experiments, 13 different masses of cylindrical strikers are used ($M = 14.1$, 21.2, 28.2, 35.3, 42.3, 49.4, 56.5, 113, 226, 339, 452, 565, 678 g). The standard deviation in experiments resulting from five measurements is 0.163 mm under 678 g heavy striker impact

$\Delta = 40.5$ mm. The numerical and experimental results agree on the low-frequency mode of oscillation of the structure and on the first 10 ms of deformation. However, the numerical model overestimates the amplitude of oscillations of the elastic guides and presents a shortened oscillation period. These discrepancies are probably due to the presence of dissipation in the soft tubes resulting from viscoelastic effects in PTFE.

We measure the maximum deflection of the system over a range of striker masses. Figure 4 reports the experimental and numerical results of the maximum deflection of the linear guides as a function of the different striker masses. We observe that the structure undergoes larger deformation as the curved granular chain is impacted with heavier masses. The largest deflection measured experimentally ($\delta = 1.86$ mm) is recorded after the structure is impacted with the heaviest striker ($M = 678$ g). The smallest deflection ($\delta = 0.027$ mm) is obtained when the structure is impacted with the lightest striker ($M = 14.1$ g). The relationship between the striker mass and the maximum deflection in the elastic guides exhibits approximately linear relationship, and we find that the difference in maximum deflections between light and heavy mass strikers is almost two orders of magnitude.

According to the classical beam theory, the strain energy stored in a beam element is proportional to the square of the maximum deflection under the condition of point or distributed loading [31]. This is under the assumption that there is no significant residual strain energy stored in the guides before the impact event. Thus, if we conjecture the squares of maximum deflection values in Fig. 4, we find that the strain energy stored in the deformed elastic guides increases steeper than the linear growth as the striker mass is increased. Given the same impact velocity for all strikers, this implies that the higher kinetic energy by large-mass striker drop results in the larger proportion of energy dispensed to the elastic guides. In other words, the elastic guides present an improved efficiency of energy absorption under large dynamic disturbances relative to that of small excitations. Such amplitude-dependent behavior can be explained by the relatively high axial stiffness of the granular chain under small impact, while the chain becomes more susceptible to buckling under the large impact, resulting from the close interplay between the granular crystal and the elastic guides. A similar trend of impact amplitude dependency can be observed in the next section by analyzing the transmitted waves measured by the force sensor mounted on the rigid wall. It should be noted that the energy absorption behavior of the deformed PTFE guides is involved with more complicated mechanisms, such as viscoelasticity, friction, and residual stress effect. Thus, the amplitude dependence of the overall system might be resolved from a more complex picture of the interplay between the granular particles and the guides.

4.2 Transmitted force profiles

After characterizing the dynamic deflection of the structure impacted with different strikers, we analyze its effects on the stress wave propagation through the granular crystals. We begin investigating the propagation of waves upon the light mass impact ($M = 14.1$ g) with a velocity of 0.443 m/s. The temporal force profiles recorded by the sensors positioned at the end of the chain are reported in Fig. 5a for the straight chain (solid

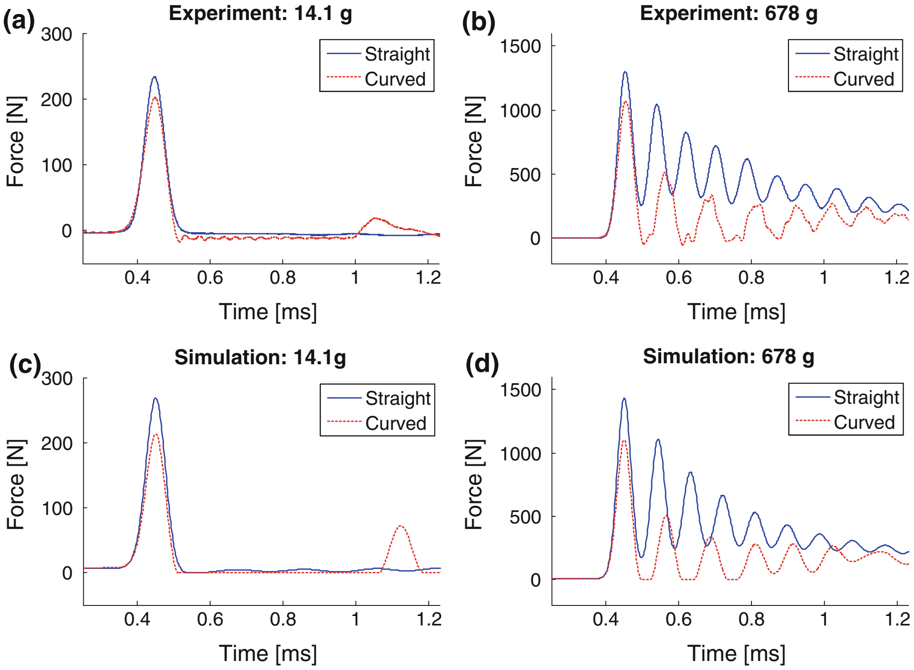

Fig. 5 Experimental (*top row*) and numerical (*bottom row*) results of the force-time profiles for the light mass (14.1 g, *left column*) and the heavy mass (678 g, *right column*) impacts. Here, the transmitted force profiles are measured from the base of the granular chains. The impact of the light mass generates a single solitary wave without significant difference between the straight and curved chains, while the impacts of heavy strikers form trains of solitary waves that show drastic changes in force profiles between the straight and curved chains

line) and curved chain (dashed line). Here, the initial offset Δ of the curved chain is 40.5 mm. For the lightest striker, which has a mass smaller than that of a bead ($m = 28.2$ g), we find that both the straight and the curved chains support the formation of a single solitary wave. This solitary wave is characterized by a compact shape (approximately 5 particle-diameter in a homogeneous chain of spherical particles) and a tunable speed of propagation, which is a function of the wave amplitude [1,2]. Comparing the responses of the straight and curved chains, we observe that the solitary wave triggered by the light striker in the curved chain is very similar to that in the straight chain. However, the maximum force reaching the end of the chain is reduced by 13.7% as compared to the straight chain (from 234 N in the straight chain to 202 N in the curved one). This is due to losses of the axial force components in the bent chain of granular particles. The area under the force-time curve, which corresponds to the amount of momentum transferred, is comparable in the straight and curved chain cases (straight chain: 1.55×10^{-2} N-s, curved chain: 1.50×10^{-2} N-s). The impulse observed at the point $\sim$ 1 ms is caused by the rebounding of the last particle in the chain, which is clamped between the sensor and the inner PTFE guides under the high curvature of the granular chain (see Fig. 2).

We then characterize the wave propagation upon the largest mass impact ($M = 678$ g). Figure 5b shows the compressive force profiles measured at the base of granular chains, in which the responses of the straight and curved chains are denoted by solid and dashed lines, respectively. Unlike the light mass impact, we observe the generation of trains of solitary waves characterized by a leading pulse with large amplitude and trailing waves with amplitudes decaying approximately exponentially [9]. However, we find that the chain of solitary waves excited in the straight and curved chains present a different behavior, when the heaviest striker impacts the chain. Comparing the force amplitudes of the leading pulses transferred through the chain, we observe that the maximum amplitude is reduced by 17.8%, from 1,301 N in the straight chain to 1,069 N in the curved one. More notably, the trailing solitary waves present amplitudes that decay faster in the curved granular chain than in the straight one. The amount of momentum transferred is significantly reduced in the curved chain (0.156 N-s) compared to that of the straight one (0.360 Ns), implying that the curved systems can more effectively attenuate signals with larger amplitudes.

Numerical results are reported in Fig. 5c, d for the small and large-mass impact. Comparing these results with the experimental ones in Fig. 5a, b, we find that the signals from the numerical simulation closely match the shape of propagating solitary waves measured in experiments. For the small mass impact in Fig. 5c, we observe that single solitary waves are formed in both straight and curved chains. In the curved chain,

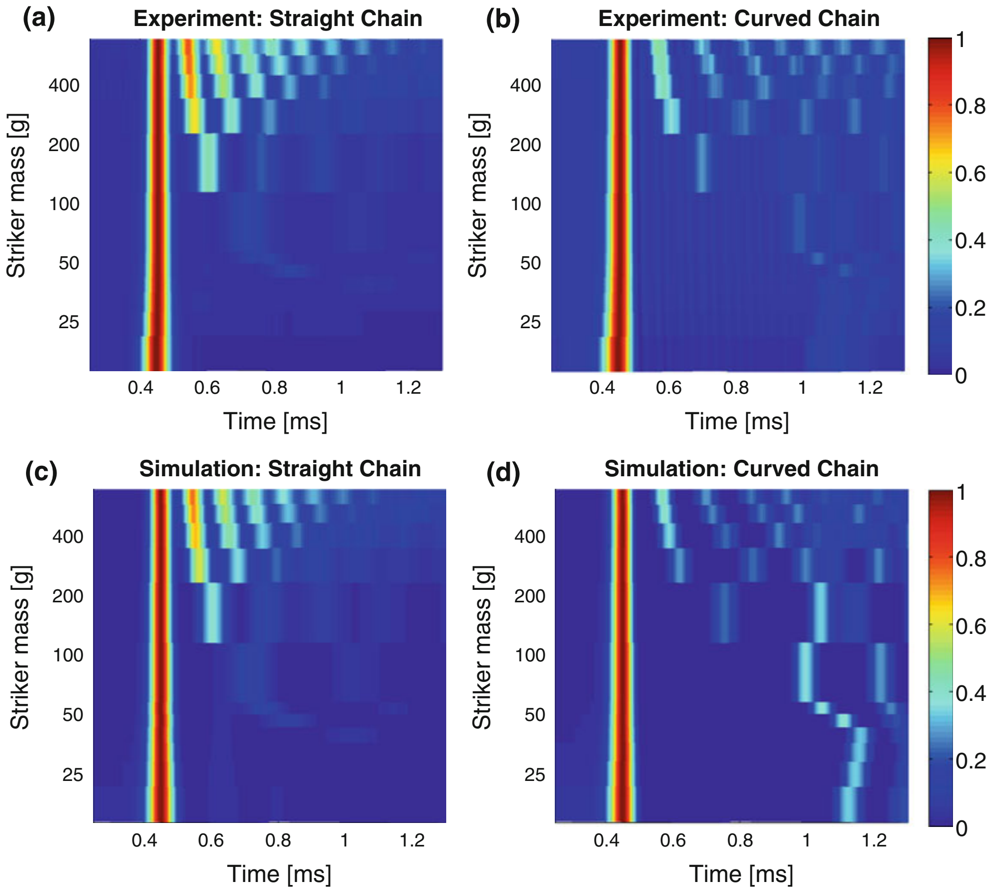

Fig. 6 Experimental (*top row*) and numerical (*bottom row*) surface plots of transmitted waves for straight (*left column*) and curved (*right column*) chains. Each surface plot depicts the force profiles of all 13 striker impacts after being normalized with respect to their maximum force amplitudes. Multiple bands of highlighted areas denote the formation of solitary wave trains, which are generated under the impacts using strikers heavier than the mass of a single bead in the chain ($M > m = 28.3$ g). Solitary wave trains in the curved chains present less intensity and sparser spacing than those in the straight chains

particularly, we successfully produce a small impulse around the point 1.1-ms, which is also witnessed in experiments in Fig. 5a. The maximum amplitudes of the simulated solitary waves tend to be larger than those in the experimental results, but the deviation is in the reasonable range (268 N in the straight chain and 213 N in the curved chain).

For the large striker impact, we observe that the numerical simulation formulates a train of solitary waves with approximately exponential decay, similar to the signals measured in experiments (compare Fig. 5b, d). These propagating waves exhibit a superposed form of high-frequency (~ 0.1-ms period) and low-frequency (millisecond order of characteristic decay time) signals. If we compare the force-time history between the straight and the curved chains, we find that the low-frequency components in the curved chain are significantly attenuated, while the high- frequency signals remain less dampened. This means that the low-frequency components of propagating waves are more efficiently absorbed by the soft elastic guides, whereas the high-frequency components are less affected by the presence of the curvature applied to the coupled system. Such higher effectiveness of shock absorption mechanism in low-frequency waves is plausible, if we consider the low-frequency bending modes of the elastic guides (see the long oscillation period of the elastic guides in Fig. 3).

Previous studies have shown that the formation of low-frequency signals (i.e., generation of a train of solitary waves) is closely associated with the mass of the striker relative to that of the particles in the chain [9]. In general, a large-mass striker can trigger the formation of a solitary wave train containing many single solitary waves, resulted from the multiple impacts at the interface between a massive striker and the granular crystal. Thus, the efficiency of the shock absorption mechanism is essentially affected by the mass of the striker. Since the striker mass also determines the amplitude of external impact, we refer to the response of the system as the amplitude-dependent characteristics in this study.

We include surface plots of the experimental and numerical results in Fig. 6, to provide a more direct comparison of the response of the straight and curved configurations. These surface plots show the transmitted force intensity in the time domain for all geometries of strikers used to generate the impulses. In these plots, each force profile is normalized with respect to its maximum amplitude, and the initial time of arrival is aligned at $t = 0.45$ ms to ease visualization. This brightest band represents the first impulse propagated along the granular chain, and the following bands denote the subsequent generation of solitary wave trains. When the straight and curved chains are impacted by a striker with a mass smaller than that of a bead (i.e., using a striker with mass $M < 28.2$ g), we observe the formation of a single solitary wave. However, when a striker with a larger mass impacts the chains, the granular crystal starts to form multiple solitary waves with decaying amplitudes. In the large-mass impact, we also find that the responses of the straight and curved configurations differ significantly. The curved chain generates a sparser train of solitary waves that travel through the chain over a more extended period of time compared to those generated in the straight chain (compare Fig. 6a, b for the experimental results and Fig. 6c, d for the corresponding numerical results).

The distinctive response of the straight and curved chains under large amplitude impacts can be explained by the energy transmission mechanism in the two geometries. In the straight chain, the compressive pulse travels primarily between the granular particles. On the contrary, in the curved configuration a significant portion of incident energy is dispensed to the confining guides via lateral interactions in the form of kinetic and strain energy of the soft PTFE tubes. From the experimental and numerical results of transmitted wave profiles, it is evident that the coupling between the nonlinear chain and the linear elastic guides becomes more dominant when the chain is impacted with larger strikers. These results are in agreement with the finding in Sect. 4.1 that the soft PTFE tubes exhibit higher energy absorption efficiency by the elastic guides under the impact with larger mass strikers.

4.3 Energy transmission

We estimate the energy transmitted through the chain and arriving on the wall by calculating the Hertzian potential energy between the last particle in the chain and the flat piezoelectric sensor located at the base of the chain. Neglecting the dissipative effect, the Hertzian potential energy (Ψ) can be expressed in terms of the compressive force $F_{N,N+1}$ between the last particle (particle index $n = N$) and the sensor ($n = N + 1$) as:

$$\Psi = \frac{2}{5}\left(A_{N,N+1}\right)^{-2/3}\left(F_{N,N+1}\right)^{5/3}. \tag{17}$$

Hence, the averaged amount of transmitted energy ($\overline{\Psi}$) over the span of time $[t_i, t_\mathrm{f}]$ can be simplified in the integral form of potential energy based on the measured discrete force profile $F[t]$ as follows:

$$\overline{\Psi} \equiv \frac{1}{t_\mathrm{f} - t_i}\int\limits_{t=t_i}^{t_\mathrm{f}} \Psi \mathrm{d}t = \frac{2}{5 f_\mathrm{s}(t_\mathrm{f} - t_i)}\sum_{t=t_i}^{t_\mathrm{f}} (A_{N,N+1})^{-2/3} F[t]^{5/3}, \tag{18}$$

where f_s is the sampling frequency of the transducer. We limit the integration time of the discrete force profiles from $t_i = 0$ ms to $t_\mathrm{f} = 1.2$ ms (see Fig. 5), to exclude the effect of the wave reflection from the striker.

We compare the energy transmission through the chains as a function of the striker geometry for four different configurations ($\Delta = 0$, 11.4, 24.1, and 40.5 mm) in Fig 7. Experimental results are shown in Fig. 7a and the corresponding numerical data are reported in Fig. 7b. From these plots, it is evident that the transmitted energy through the straight chain is almost linear (line with open circles), implying that in the straight configuration the transmitted waves carry the impact energy without significant dissipation [1,2]. The energy transmitted through the curved chains instead shows a clear dependence on the striker mass. As the striker mass is increased, the energy transmitted is decreased compared with the straight configuration. Notably, the amount of energy transmitted can be reduced by imposing a larger initial curvature to the chains. This allows tuning the amount of energy loss into the guides in the form of strain and kinetic energy. The numerical results are found in good agreement with the experimental data.

We quantify the energy transmission efficiency of the curved chains with respect to that of the straight chain in Fig. 8. Here, the experimental and numerical ratios of transmitted energy are plotted as a function

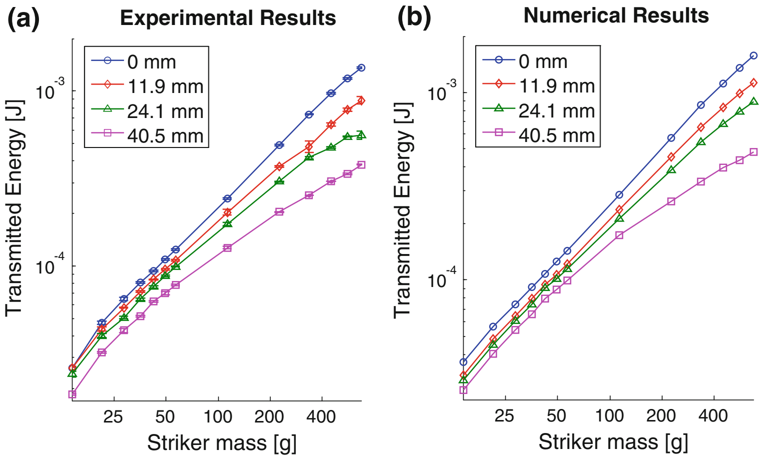

Fig. 7 Experimental (*left*) and numerical (*right*) results of transmitted energy through the granular chain as a function of striker masses. The chain configurations tested include a straight chain ($\Delta = 0$ mm) and three curved chains ($\Delta = 11.9, 24.1, 40.5$ mm). *The error bars* in the experimental results denote standard deviations from five measurements of the energy values per chain curvature and striker mass

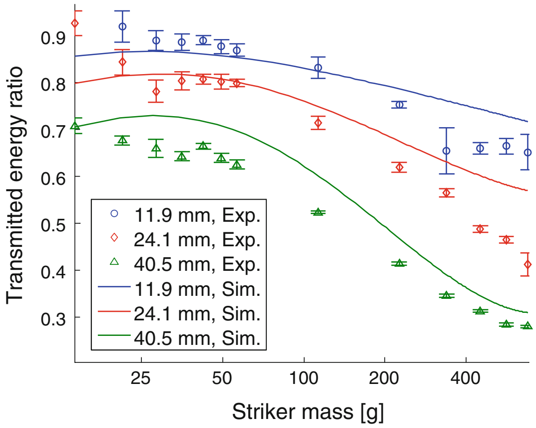

Fig. 8 The ratios of the curved chain's transmitted energy values to those of the straight chain as a function of striker masses. *The dotted lines* represent numerical results, while the discrete points with *error bars* denote experimental results. As striker masses increase, the transmitted energy ratios decrease accordingly, showing amplitude-dependent energy transmitting properties. A more drastic reduction of the transmitted energy ratios is obtained for the granular chain with larger curvatures

of the different striker masses used for the impacts. From experiments, we find that a curved chain exhibits high transmission efficiency in the range between approximately 70 and 90% under small disturbances, while the efficiency drops as low as 25% when the chains are impacted with larger strikers. The experimental and numerical results are in fair agreement. This translates into the amplitude-dependent energy transmission efficiency in the combined system of granular crystals and curved elastic guides. More notably, we find that the energy transmission efficiency depends on the curvature imposed to the system. For the smallest curvature ($\Delta = 11.4$ mm), we observe experimentally that the energy transmission ratio changes between 65 and 92%, given the various striker masses (top curve in Fig. 8). If the curvature of the system is increased to $\Delta = 40.5$ mm, the variation of the energy transmission ratio becomes more drastic (28–71%), as the striker mass varies from 14.1 to 678 g. In Fig. 8, we observe that the experimental ratios lie below the numerical ones for larger disturbances. This is probably due to the increased effects of friction and viscoelasticity when the system is excited with larger strikers.

The numerical and experimental results in this study show that the amplitude-dependent transmission of compressive waves can be achieved in a regenerative manner, using the combined system of granular crystals and linear elastic media. In addition, the energy transmission efficiency can be controlled by manipulating the curvature of the combined system of granular crystal and the elastic guides. It is important to mention that no visible onset of permanent deformation in the particles or structural buckling is observed in the range of impacts tested in this study.

5 Conclusion

In this study, we describe the wave propagation in straight and curved granular chains confined by linear elastic guides using experiments and numerical simulations. We show that the force and energy transmission through these systems is controlled by the initial deflection of the chains. Furthermore, we demonstrate that impacts generated by strikers with a smaller mass can travel through the granular chains without major losses, while impacts generated by larger strikers are partially absorbed by the flexible supporting structure in the form of strain and kinetic energy. This interplay between the granular crystal and the confining linear media is validated from both the deflection profiles of PTFE supports obtained from high-speed photography and the compressive wave measurements from the force sensor at the base of the granular chains. The energy transmission through the curved granular crystal is shown to exhibit a nonlinear trend with respect to the amplitudes of the external impacts. This experimental and numerical study shows that a hybrid structure composed of a nonlinear granular crystal and deformable supporting guides can be used to selectively allow or reduce the transmission of compressive excitations, as a function of their amplitude. The efficiency of transmission can be tuned by variation of the initial curvature imposed to the system. We expect that a similar behavior will persist in smaller scale hybrid linear-nonlinear systems, and in specifically designed two- and three-dimensional structures. Such materials could be used for selective acoustic filtering devices, impact protection systems, and amplitude-dependent vibration absorption layers.

Acknowledgments We acknowledge the support of DARPA (Contract N. HR0011-10-C-0089, Dr. Jinendra Ranka) and the National Science Foundation, Grant Number CMMI-0844540 (Career). We also thank Stephane Job for helpful comments.

References

1. Nesterenko, V.F.: Dynamics of Heterogeneous Materials. Springer, New York (2001)
2. Sen, S., Hong, J., Bang, J., Avalos, E., Doney, R.: Solitary waves in the granular chain. Phys. Rep. **462**, 21–66 (2008)
3. Daraio, C., Nesterenko, V.F., Herbold, E.B., Jin, S.: Tunability of solitary wave properties in one-dimensional strongly nonlinear phononic crystals. Phys. Rev. E Stat. Nonlin. Soft. Matter Phys. **73**, 026610 (2006)
4. Hladky-Hennion, A.C., de Billy, M.: Experimental validation of band gaps and localization in a one-dimensional diatomic phononic crystal. J. Acoust. Soc. Am. **122**, 2594–2600 (2007)
5. Coste, C., Falcon, E., Fauve, S.: Solitary waves in a chain of beads under Hertz contact. Phys. Rev. E **56**, 6104–6117 (1997)
6. Daraio, C., Nesterenko, V.F., Herbold, E.B., Jin, S.: Strongly nonlinear waves in a chain of Teflon beads. Phys. Rev. E **72**, 016603 (2005)
7. Daraio, C., Nesterenko, V.F., Herbold, E.B., Jin, S.: Energy trapping and shock disintegration in a composite granular medium. Phys. Rev. Lett. **96**, 058002 (2006)
8. Shukla, A., Sadd, M.H., Xu, Y., Tai, Q.M.: Influence of loading pulse duration on dynamic load transfer in a simulated granular medium. J. Mech. Phys. Solids **41**, 1795–1808 (1993)
9. Job, S., Melo, F., Sokolow, A., Sen, S.: Solitary wave trains in granular chains: experiments, theory and simulations. Granul. Matter **10**, 13–20 (2007)
10. Boechler, N., Yang, J., Theocharis, G., Kevrekidis, P.G., Daraio, C.: Tunable vibrational band gaps in one-dimensional diatomic granular crystals with three-particle unit cells. J. Appl. Phys. **109**(7), 074906 (2011)
11. Manciu, M., Sen, S., Hurd, A.J.: Crossing of identical solitary waves in a chain of elastic beads. Phys. Rev. E **63**, 016614 (2001)
12. Spadoni, A., Daraio, C.: Generation and control of sound bullets with a nonlinear acoustic lens. Proc. Natl. Acad. Sci. USA. **107**, 7230–7234 (2010)
13. Khatri, D., Rizzo, P., Daraio, C.: Highly Nonlinear Waves' Sensor Technology for Highway Infrastructures. In: Proceeding for SPIE Smart Structures/NDE, pp. 6934–6925 (2008)
14. Ni, X., Rizzo, P., Daraio, C.: Actuators for the generation of highly nonlinear solitary waves. Rev. Sci. Instrum. **82**, 034902–034906 (2011)
15. Hong, J.B., Xu, A.G.: Nondestructive identification of impurities in granular medium. Appl. Phys. Lett. **81**, 4868–4870 (2002)
16. Vakakis, A.F. (ed.): Normal Modes and Localization in Nonlinear Systems. John Wiley and Sons, New York (1996)
17. Theocharis, G., Kavousanakis, M., Kevrekidis, P.G., Daraio, C., Porter, M.A., Kevrekidis, I.G.: Localized breathing modes in granular crystals with defects. Phys. Rev. E. Stat. Nonlin. Soft. Matter Phys. **80**, 066601 (2009)
18. Daraio, C., Nesterenko, V.F.: Propagation of highly nonlinear signals in a two dimensional network of granular chains. Shock Compress. Condens. Matter **955**(Pts 1 and 2), 1419–1422 (2007)
19. Daraio, C., Ngo, D., Nesterenko, V.F., Fraternali, F.: Highly nonlinear pulse splitting and recombination in a two-dimensional granular network. Phys. Rev. E **82**, 036603 (2010)
20. Doney, R.L., Sen, S.: Impulse absorption by tapered horizontal alignments of elastic spheres. Phys. Rev. E **72**, 041304 (2005)

21. Job, S., Melo, F., Sokolow, A., Sen, S.: How Hertzian solitary waves interact with boundaries in a 1D granular medium. Phys. Rev. Lett. **94**, 178002 (2005)
22. Rosas, A., Romero, A.H., Nesterenko, V.F., Lindenberg, K.: Observation of two-wave structure in strongly nonlinear dissipative granular chains. Phys. Rev. Lett. **98**, 164301 (2007)
23. Carretero-González, R., Khatri, D., Porter, M.A., Kevrekidis, P.G., Daraio, C.: Dissipative solitary waves in granular crystals. Phys. Rev. Lett. **102**, 024102 (2009)
24. Mindlin, R.D.: Compliance of elastic bodies in contact. J. Appl. Mech. **16**, 259–268 (1949)
25. Johnson, K.L.: Contact Mechanics. Cambridge University Press, Cambridge (1985). The maximum contact pressure developed beneath the contact surface is estimated to be 2,424 MPa, given the geometries and masses of the sphere and cylindrical striker made of 440C stainless steel. This is smaller than 1.60Y, where Y is the yield stress of the 440C material (1.60Y = 3,034 MPa), implying no onset of plasticity effect
26. Cundall, P.A., Strack, O.D.L.: A discrete numerical model for granular assemblies. Geotechnique **29**, 47–65 (1979)
27. Tsuji, Y., Tanaka, T., Ishida, T.: Lagrangian numerical simulation of plug flow of cohesionless particles in a horizontal pipe. Powder Technol. **71**, 239–250 (1992)
28. Yang, J., Silvestro, C., Khatri, D., De Nardo, L., Daraio, C.: Interaction of highly nonlinear solitary waves with linear elastic media. Phys. Rev. E. **83**, 046606 (2011)
29. Gonzalez, R.C., Woods, R.E.: Digital Image Processing. Prentice-Hall, Upper Saddle River (2008)
30. Kattan, P.I.: MATLAB Guide to Finite Elements: An Interactive Approach. Springer, New York (2007)
31. Gere, J.M., Timoshenko, S.P.: Mechanics of Materials. Pws Pub Co., Boston (1997)
32. Reed, J.: Energy losses due to elastic wave propagation during an elastic impact. J. Phys. D Appl. Phys. **18**, 2329–2337 (1985)
33. Hunter, S.C.: Energy absorbed by elastic waves during impact. J. Mech. Phys. Solids **5**, 162–171 (1957)
34. Lorenz, A., Tuozzolo, C., Louge, M.Y.: Measurements of impact properties of small, nearly spherical particles. In: Second International Conference on CFD in the Minerals and Process Industries, vol. 37, pp. 292–298 (1997)
35. Puttock, M.J., Thwaite, E.G.: Elastic compression of spheres and cylinders at point and line contact. In: National Standards Laboratory Technical Paper No. 25, Commonwealth Scientific and Industrial Research Organization. Australia (1969)
36. Shampine, L.F., Reichelt, M.W.: The MATLAB ODE Suite. SIAM J. Sci. Comput. **18**, 1–22 (1997)